Geochemistry, Geophysics, Geosystems®

RESEARCH ARTICLE
10.1029/2021GC010062

A New Method for Determining Fluid Flux at High Pressures Applied to the Dehydration of Serpentinites

L. Eberhard[1,2], M. Thielmann[1], P. Eichheimer[1,3], A. Néri[1], A. Suzuki[4], M. Ohl[2], W. Fujita[4], K. Uesugi[5], M. Nakamura[4], G. J. Golabek[1], and D. J. Frost[1]

[1]Bayerisches Geoinstitut, University of Bayreuth, Bayreuth, Germany, [2]Department of Earth Sciences, Utrecht University, Utrecht, The Netherlands, [3]Math2Market GmbH, Kaiserslautern, Germany, [4]Department of Earth Science, Tohoku University, Sendai, Japan, [5]Japan Synchrotron Radiation Research Institute (JASRI/Spring-8), Hyogo, Japan

Abstract A new method to determine fluid flux at high pressures and temperatures has been developed and used to study serpentinites at subduction zone conditions. Drill cores of a natural antigorite-serpentinite with a strong foliation were used in multi-anvil experiments in the range of 2–5 GPa and 450–800°C. Fluids released upon dehydration are fixed by the formation of brucite in an adjacent fluid sink. The amount and distribution of brucite serves as a proxy for fluid flow. In our specific setup the sample reacted with the surrounding fluid sink to form an additional layer of olivine, which has the potential to limit fluid flux within our experiments. For conditions prior to serpentine dehydration we used $Al(OH)_3$ as fluid source. Fluid in this experiment did not migrate through the serpentinite, indicating that serpentine has a low diffusivity. The experiments also show that small deviatoric stresses have an influence on the fluid flux and can cause an anisotropic fluid flux. Comparison between the time scales of the determined fluid flux with fluid production rates indicates fluid pressure buildup during dehydration reactions. Adjacent less permeable layers can inhibit fluid flux and cause fluid pressure buildup even at conditions when an interconnected pore space formed.

Plain Language Summary Subduction zones are regions where tectonic plates are recycled into the Earth's interior. Prior to subduction, the plates experienced extensive chemical interaction with the ocean water, forming hydrous minerals. Serpentine is an important hydrous mineral that can transport significant amounts of water into the Earth's interior. During subduction both pressure and temperature increase whereby hydrous minerals break down and release their water. The fluid migrates into the overlying mantle wedge, where it accounts for hydration as well as melting processes. The global flux balances would require this process to be very effective. However, it was so far not possible to measure the fluid flux at the subduction zone conditions in laboratories. In this study, we present a new method to determine the fluid flux prior and during dehydration. We found that prior to dehydration, the fluid flux in serpentinites is small. During dehydration the rocks ability to let fluids pass through increases. However, adjacent rocks with a low ability for fluid transport can further inhibit a fluid flux at these conditions. Generally, our experimental setup can be used for any system that immobilizes migrating fluids by hydration reactions.

Key Points:

- A new method to determine fluid flux at high pressure and temperature conditions is developed
- Slow fluid migration in serpentinites promotes brittle fracturing in subduction zones
- Fast fluid migration upon dehydration of serpentinites promotes large-scale fluid flux, if not inhibited by adjacent less permeable layers

Supporting Information:

Supporting Information may be found in the online version of this article.

Correspondence to:

L. Eberhard,
l.eberhard@uu.nl

Citation:

Eberhard, L., Thielmann, M., Eichheimer, P., Néri, A., Suzuki, A., Ohl, M., et al. (2022). A new method for determining fluid flux at high pressures applied to the dehydration of serpentinites. *Geochemistry, Geophysics, Geosystems*, *23*, e2021GC010062. https://doi.org/10.1029/2021GC010062

Received 26 JUL 2021
Accepted 4 AUG 2022

1. Introduction

The transport of water in subduction zones from the Earth's surface into the interior plays an important role in many arc-related processes. The release of water from the subducting lithosphere causes element mobility and metasomatism of the overlying mantle wedge, lowers the melting temperature of mantle rocks, raises the degree of arc mantle melting and may be involved in the origin of at least some intermediate-depth earthquakes (Grove et al., 2006; Peacock, 1990; Reynard, 2013; Schmidt & Poli, 2014). The annual flux of subducted water has been estimated in various studies and ranges between 0.1×10^{12} and 3×10^{12} kg yr^{-1} (Cai et al., 2018; Korenaga, 2017; Magni et al., 2014; Rüpke et al., 2004; van Keken et al., 2011). In order to balance global water fluxes about two thirds of the subducted water is expected to be released from the slab into the mantle wedge and return back to the Earth's surface (van Keken et al., 2011). It has been argued that such efficient recycling requires released fluids to rapidly organize into channelized networks rather than undergoing unfocused grain scale pervasive fluid flow controlled by rock permeability (Plümper, Botan, et al., 2017; Plümper, John, et al., 2017).

The nature of the fluid flux will also have implications for the removal through dissolution of important volatile components including carbon and sulfur. For example, fluids released in subduction zones have the potential to

transport significant amounts of dissolved carbonate species, from the slab toward the mantle wedge (Gorman et al., 2006; Kelemen & Manning, 2015; Menzel et al., 2019; Tian et al., 2019). The extent of carbonate dissolution, however, will vary strongly depending on whether channelized or pervasive flow occurs, as a pervasive fluid flux will affect a much larger rock volume. The mode of fluid flux will be influenced by mineralogical and textural characteristics of the slab and overlying mantle. Deep-rooted normal faults, caused by bending of the subducting plate, may form zones of distinctively higher permeability (Arnulf et al., 2022; Faccenda et al., 2009; Korenaga, 2017). Certain lithologies may also be relatively impermeable or possess strong foliation that may focus fluid flow between the foliated layers and limit the flux into the mantle wedge (Kawano et al., 2011). Experiments performed at low pressures and temperatures, for example, indicate that strongly foliated serpentine leads to an anisotropic fluid flux, where the flux parallel to the foliation direction is almost two orders of magnitude higher than normal to the foliation (Kawano et al., 2011; Okazaki et al., 2013).

In order to understand the direction and magnitude of the fluid flux from subducting slabs it is necessary to be able to determine the fluid transport mechanisms and magnitude through the respective lithological assemblages. In low porosity rocks, the fluid transport may be described with respect to diffusion (Fick's first law):

$$q_x = -D\,\mathrm{d}C/\mathrm{d}x, \tag{1}$$

where q is the fluid flux, D *is* the diffusion constant, and $\mathrm{d}C/\mathrm{d}x$ *is* the concentration gradient. Alternatively, fluid transport in porous media may be described by Darcy's law:

$$q_x = -(k/\eta)\,\mathrm{d}P/\mathrm{d}x, \tag{2}$$

which relates the fluid flux to the permeability k, the fluid viscosity η, and the pressure gradient $\mathrm{d}P/\mathrm{d}x$. The pressure range of conventional laboratory permeability measurements is limited to conditions at which a fluid overpressure can be maintained, that is, a few hundred megapascal. Permeability measurements on high grade rocks are consequently performed at pressures lower than peak metamorphic conditions (Kawano et al., 2011; Okazaki et al., 2013; Tenthorey & Cox, 2003). At low pressures permeability depends on the pore space geometry, which in turn depends on rock texture and strength. Studies on continental drilling sites indicate a decrease in permeability with increasing depth as porosity closes (Manning & Ingebritsen, 1999). Once metamorphic conditions are reached permeability will depend strongly on the wetting behavior of grain boundaries but aside from measurements of mineral-fluid dihedral angles (Huang et al., 2019, 2020) methods are lacking for determining fluid fluxes at sub arc conditions.

Tenthorey and Cox (2003) showed that during dehydration processes the permeability increases by two orders of magnitude due to the formation of pore space. Dehydration reactions can also change the local pressure and thereby suppress the progress of the reaction (Fusseis et al., 2012). On the other hand, mineral reactions can form nanopores which, once filled with fluid, create a local chemical gradient that may drive the reaction forward (Plümper, Botan, et al., 2017; Plümper, John, et al., 2017). Natural rocks are further affected by textural changes that occur through retrograde processes (Li et al., 2004), including mineral reactions, metasomatism, and deformation. The rocks texture observed in laboratories is thus different from its high pressure and temperature (PT) texture so that permeabilities measured may not be applicable to their higher pressure origins. It is thus crucial to have a method to determine the fluid flux in rocks at high PT conditions.

In this study, we present a new and simple technique to determine fluid flux at high PT conditions, from which we can estimate both diffusivities and permeabilities (Equations 1 and 2). We employ this method to investigate serpentinite rocks before and during dehydration at subduction zone conditions. Additionally, we use X-ray micro computed tomography to analyze compaction due to fluid migration and verify our experimental results. The results indicate that the fluid production rate during the dehydration of serpentinites will be significantly higher with respect to both relaxation of the sample and the fluid flux. Our specific system also leads to interaction between the sample and the surroundings, revealing important effects of adjacent rock layers on the fluid migration.

2. Materials and Methods

The method relies on trapping the fluid released by a dehydration reaction at high *PT* conditions in material surrounding the sample through the formation of a hydroxide, which is stable at the temperature of the investigated dehydration reaction. We use adjacent serpentine (fluid source) and MgO (fluid sink) to evaluate the fluid flux at elevated *PT* conditions. The stable serpentine polymorph at high *PT* conditions is antigorite $(Mg,Fe,Al)_{48}(Si,Al)_{34}O_{85}(OH)_{62}$. With increasing temperature, a series of dehydration reactions occurs in serpentinites, which are at 3 GPa:

$$\sim 450°C: \text{brucite} + \text{antigorite} = \text{olivine} + H_2O \quad (3)$$

$$\sim 650°C: \text{antigorite} = \text{olivine} + \text{pyroxene} + \text{chlorite} + H_2O \quad (4)$$

$$\sim 800°C: \text{chlorite} = \text{olivine} + \text{pyroxene} + \text{garnet/spinel} + H_2O \quad (5)$$

In complex natural systems, which include aluminum and iron, reactions (3–5) are divariant and occur over a temperature interval (Merkulova et al., 2016; Padrón-Navarta et al., 2013), throughout which the fabric of the sheet silicates, antigorite and chlorite, still have the potential to control the direction of the fluid flow. In our experiments a cylindrical serpentinite sample is placed adjacent to sintered polycrystalline MgO. As the released fluids infiltrate this material they are immobilized through the formation of brucite,

$$MgO + H_2O = Mg(OH)_2. \quad (6)$$

The proportion of brucite can then be used to constrain the time-integrated fluid flux out of the sample. In contrast to reaction (3), in the absence of other silicate minerals the brucite stability field extends up to 1,000°C at 3 GPa (Johnson & Walker, 1993; Okada et al., 2002), well above the antigorite dehydration temperature at pressures relevant for subduction zones. To determine the fluid transport through serpentinites prior to dehydration, $Al(OH)_3$ was employed as an external fluid source in a further modified experiment.

2.1. Starting Material

The starting material used in the experiments is an antigorite-serpentinite from Zermatt (45° 58.16' N, 7° 42.566' E). The sample was characterized using optical microscopy, Raman spectroscopy, and electron microprobe analyses (EMPA). The antigorite-serpentinite consists of >95% antigorite and <5% magnetite and minor sulphides (<1%, not further distinguished). The presence of a few individual grains of Ti-clinohumite and clinopyroxene was confirmed by EMPA. HCl-tests confirmed the absence of carbonates. Antigorite is fine-grained (<1 mm) and shows a strong shape preferred orientation. The overall texture is similar to mylonitic serpentinites described in Li et al. (2004), representing high strain rocks caused by deformation during subduction and obduction stages.

Drill cores of 1.5 mm radius and 1.5 mm length were prepared from the sample. The drill core axis was orientated parallel or perpendicular to the serpentine foliation (Table 1). A first order quantification of the preferred orientation of the drill cores was obtained using scanning electron microscopy (SEM) (see also Section 2.3) and later confirmed on representative samples using electron back-scattered diffraction.

2.2. High Pressure Experiments

High pressure experiments were performed in a Walker-type multi-anvil apparatus at the Bayerisches Geoinstitut (BGI) and a split-cylinder multi-anvil apparatus at Tohoku University (TU). The pressure was calibrated with bismuth phase transitions at room temperature and the quartz-coesite transition at 700°C (Bose & Ganguly, 1995). A type D-thermocouple was used to monitor the temperature and temperature-power correlations were used in case of thermocouple failure. All experiments were ramped to target pressure within ≈3 hr and subsequently heated to the target temperature. The pressure was released after quenching within at least 15 hr.

In a first set of experiments (SETUP I) an intrinsic fluid source was used to determine the fluid flux. In these experiments the serpentine drill cores were placed inside an MgO sleeve prepared from sintered polycrystalline MgO. The MgO sleeve consists of a hollow cylinder of 3.6 mm outer diameter covered at the top and bottom with 0.8 mm thick MgO discs (Figure 1a). The samples were welded into 4 mm diameter gold capsules and run

Table 1
Experimental Conditions and Run Product Mineralogy as Obtained From SEM Analyses

Sample	T (°C)	P (GPa)	t (h)	Orientation	Phases	Mechanism
V1149	550	2	24	⊥	Atg, Mag	–
V1152	700^{+}	2	24	⊥	Atg, Mag	Solid-state
ES367	800^{+}	2.5	0.5	⊥	Chl, Ol, Opx, Mag	Fluid-induced
ES369	700	2.5	1	⊥	Atg, (Ol, O), Mag	Solid-state
ES372	800^{+}	2.5	0.5	⊥	Atg, Ol, Opx, Mag	Fluid-induced
V1155	700^{+}	2	6	⊥	Atg, (Ol, Opx), Mag	Solid-state
V1156	800	3.5	6	⊥	Ol, Opx, Grt	Fluid-induced
V1157	450^{+}	3.5	6	⊥	Atg, Mag	–
V1163	650	2	216	⊥	Atg, (Ol, Opx), Mag	Solid-state
V1165	650	2	96	⊥	Atg, (Ol, Op), Mag	Solid-state
V1166	700	2	96	⊥	Chl, Ol, Opx, Mag	Fluid-induced
V1167*	720	2	24	⊥	Chl, Ol, Opx, Mag	–
V1170*	500^{+}	2	96	//	Atg, Chl	–
V1171	650	2	96	//	Atg, (Ol, Opx), Mag	Solid-state
V1172	700	2	216	⊥	Chl, Ol, Opx, Mag	Fluid-induced
V1175	700	2	96	//	Chl, Ol, Opx, Mag, Cpx	Fluid-induced
V1188	750	2	24	⊥	Chl, Ol, Opx, Mag	Fluid-induced
V1189	700^{+}	2	48	⊥	Chl, Ol, Opx, Mag	Fluid-induced
V1203	750	2	12	⊥	Chl, Ol, Opx, Mag	Fluid-induced
V1210	700	2	1	⊥	Atg, Mag	Solid-state
V1211	750	2	72	⊥	Chl, Ol, Opx, Mag	Fluid-induced
V1214	800	5	24	⊥	Ol, Opx, Grt	Fluid-induced

Note. Time refers to time at target pressure and temperature conditions. The chemical compositions of phases are given in the supporting information S1 (Table A-1). Orientation refers to the direction of the drill core axis with respect to the foliation of serpentine: ⊥ marks perpendicular, // marks parallel orientation. Mechanism indicates whether brucite was formed through fluids released from antigorite (fluid-induced) or from the solid-state reaction described in the main text. Samples marked with * are 18/11 experiments. Temperatures are based on thermocouple measurements and on power-temperature correlations in case of thermocouple failure, the latter are marked with $^{+}$. Phases in brackets were observed but were too small for chemical analyses. Mineral abbreviations after Whitney and Evans (2010).

in 25/17 (octahedral edge length/truncation edge length) standard BGI assemblies (Keppler & Frost, 2005). One experiment, V1214, was run in a 25/15 assembly in order to reach a higher pressure. During the experiment fluid released through dehydration reactions (4) and (5) migrated into the MgO sleeve and formed brucite all around the serpentine drill core (compare Figures 4a and 4b). From the thickness of the brucite layer in axial and radial directions, the fluid flux in the respective directions could be obtained.

In experiment V1167, the serpentinite drill core was welded in a 2 mm AuPd capsule without surrounding MgO and run in an 18/11 assembly. The aim of this experiment was to keep the fluid inside the serpentine drill for X-ray micro computed tomography (μCT) measurements. By comparing this experiment to experiments using an MgO fluid sink, it is possible to explore the pore space reduction caused by the fluid migration.

To determine the fluid flux through serpentinites prior to the onset of dehydration an external fluid source was used in experiment V1170 (SETUP II). The serpentine drill core was placed into a 2 mm AuPd capsule and run in 18/11 assemblies (Figure 1b). Below the drill core gibbsite $Al(OH)_3$ powder was placed. At ambient pressure gibbsite, the most available $Al(OH)_3$ polymorph, dehydrates gradually to AlO(OH) between 200°C and 400°C and further to Al_2O_3 between 450°C and 600°C (Mercury et al., 2006). It thus serves as an external fluid source at conditions where antigorite is still stable. An MgO disc prepared from sintered polycrystalline MgO atop the drill core serves as a fluid sink in this experiment.

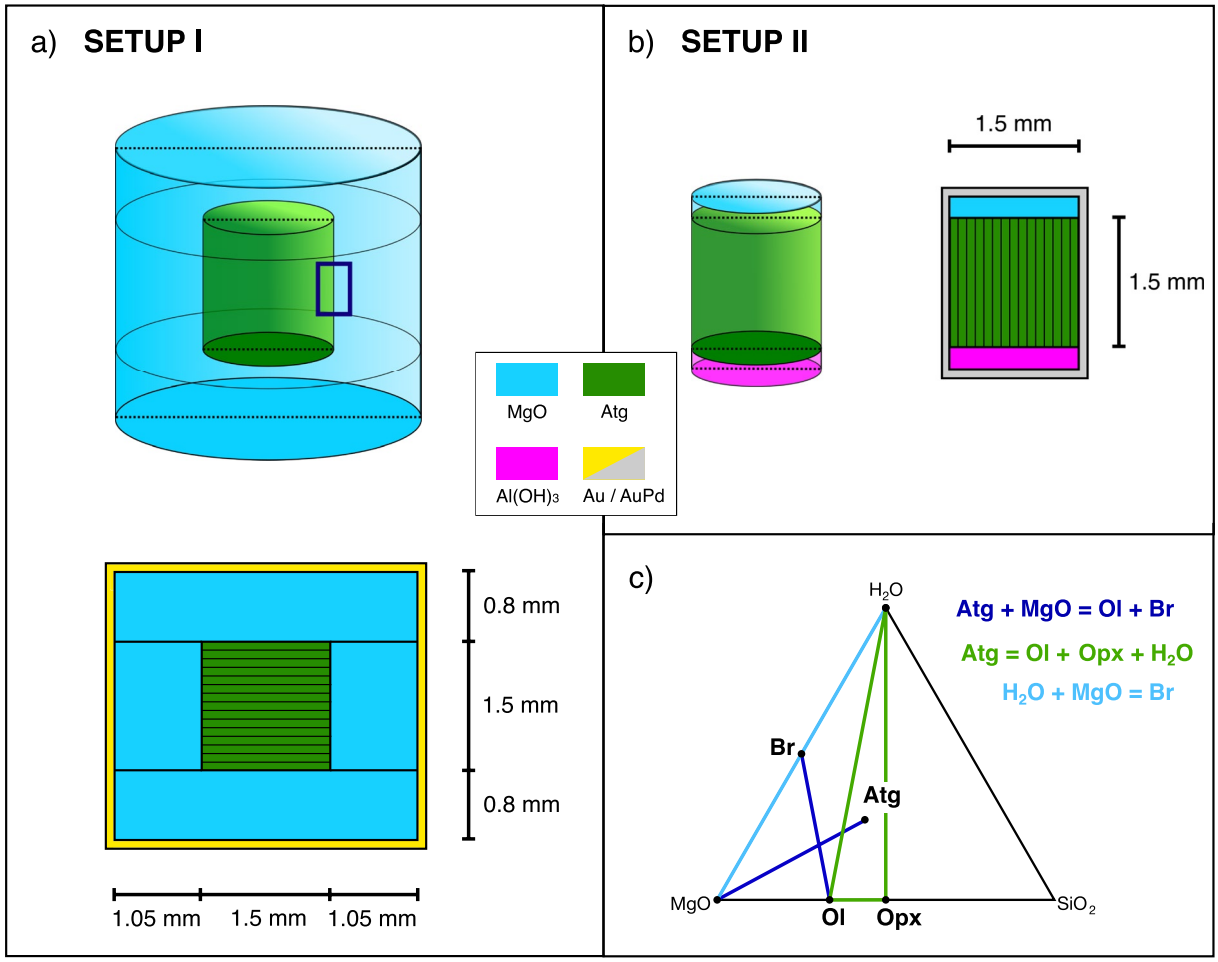

Figure 1. (a) First set of experiments (SETUP I): A serpentinite drill core is embedded into an MgO sleeve. The blue rectangle marks the position of secondary electron images shown in Figure 5. Parallel lines through the sample indicate the orientation of the foliation, which in this example is perpendicular to the dril axis (Table 1). (b) In SETUP II the serpentine drill core is sandwiched between an $Al(OH)_3$ water source and an MgO water sink. The orientation in this experiment was parallel (Table 1). The dotted line indicates position of the section prepared for further analyses. (c) General phase relations in the MSH-system. The three main reactions are the solid-state reaction between antigorite and MgO (brown), the antigorite dehydration (green), and the MgO hydration (blue).

Experiments were carried out at pressures ranging from 2 to 5 GPa and temperatures from 450°C to 800°C. To better understand reaction kinetics in our system, we also varied the time for experiments run at similar conditions. The time at target conditions varied from 0.5 to 216 hr as indicated in Table 1. All recovered run products were mounted in epoxy and polished for SEM and EMPA. During polishing care was taken to polish exactly to the middle of the sample (indicated as a dotted line in Figures 1a and 1b) that is defined optically based on the diameter of the drill core. Any assessment of the brucite layer thicknesses formed in the experiments using a section other than from the middle of the sample would be significantly distorted due to the cylindrical geometry, thus preventing a meaningful comparison between samples.

2.3. Analytical Methods

First order phase identification of run products was performed by energy-dispersive X-ray analyses with a GEMINI LEO 1530 scanning electron microscope at the BGI, operating at 20 kV. Most experiments showed a double layer of monomineralic brucite and olivine surrounding the drill core, which will be discussed in detail in Section 3.3. The thickness of these layers was determined from secondary electron (SE) images. The total area of each layer was quantified with the histogram tool of the open source software GIMP 2.8.14. By dividing the total area by the length, we obtained the mean thickness of each layer (Table A-3 in Supporting Information S1). In order to obtain suitable statistics, several SE images on each side of the drill core were taken with different

magnifications. The thicknesses obtained for the same sample using different magnifications were compared to each other in order to exclude a magnification bias.

For two representative experiments, V1152 (hydrated) and V1156 (dehydrated), the crystallographic preferred orientation (CPO) of the stable phases was analyzed by electron backscattered diffraction (EBSD). EBSD measurements were performed at the University of Utrecht with a GEMINI 450 SEM, equipped with an Oxford Instruments Symmetry detector. The sample surface was polished with a colloidal silica suspension for 15 min. Both samples were measured in 20 Pa environmental pressure without coating. The antigorite sample was measured employing a 20 kV acceleration voltage and 10 nA beam current. The dehydrated sample was measured at 25 kV acceleration voltage and 20 nA. Indexing was performed with the AZTEC software from Oxford Instruments. For antigorite, the lattice constant *a* was manually changed to 82 Å to obtain the best possible matching. Data treatment was performed with the CHANEL5 software package and polefigures were created using the open-source Matlab code MTEX (Bachmann et al., 2010).

Quantitative EMPA were performed using a JEOL 8200 microprobe with an acceleration voltage of 15 kV. Calibrations were performed using silicates, oxides, and metals. A San Carlos olivine was measured in each session for internal consistency. Operating conditions were tuned for each phase as follows: for antigorite and chlorite a 10–15 nA beam current and a 3 μm beam diameter were used, while a 15 nA beam current and <1 μm beam diameter were employed for olivine, pyroxene, garnet, and magnetite.

The pore space preserved within two recovered samples was measured using μCT-scans at the BL20XU experimental hutch two of the SPring-8 synchrotron facility (Uesugi et al., 2012). The μCT-scans were taken on sample ES376 (SETUP I) and V1167 (SETUP II without $Al[OH]_3$ and MgO). We used the software GeoDict (Becker et al., 2020) for data processing and permeability determination. Details on data collection and processing can be found in the Text B-2 in Supporting Information S2.

Mass balance calculations were performed on the run products (Table 1) to determine mineral and fluid proportions. Since magnetite, sulphides, the Mg-silicates diopside, and Ti-clinohumite were not observed in each sample and did not contribute to the dehydration reactions, they were excluded from the mass balance. The fluid is assumed to be pure H_2O, given the generally low content of dissolved major elements in fluids released from serpentinites at high *PT* conditions (Menzel et al., 2020). We used a Monte Carlo simulation to estimate uncertainties. For this purpose 1,000 individual minimizations were performed with both the starting material and run product composition randomly sampling around their normal distribution. Reported in the Table A-1 in Supporting Information S1 are mean values and the 1σ standard deviation of the simulations.

3. Results

3.1. Phase Relations

The run products obtained in each experiment are summarized in Table 1 and cover the temperature range of antigorite dehydration to garnet + olivine + orthopyroxene + fluid. At the onset of dehydration, fine-grained magnesium silicates (expected to be olivine and orthopyroxene based on thermodynamic calculations, see also Figure 3) are formed along the grain boundaries of antigorite and around individual grains of magnetite and clinopyroxene (Figure 2a). As dehydration proceeds, patches of olivine and orthopyroxene are observed with antigorite flakes in between (Figure 2b). In experiment ES372, these patches formed mainly in an hourglass shaped region at the rim of the drill core, whereas at the top and bottom antigorite remains the main phase. At temperatures >650°C the fraction of olivine and orthopyroxene further increases and chlorite is observed instead of antigorite (Figure 2c). At this stage of dehydration all phases are distributed homogenously and we could not observe a gradient in reaction process over the samples. Fully dehydrated experiments performed at $T > 800$°C and $P \geq 3.5$ GPa also contained garnet (Figure 2d), which is observed only along the interface of the drill core and the MgO sleeve. These general phase relations are in agreement with previously published studies (Bromiley & Pawley, 2003; Merkulova et al., 2016; Ulmer & Trommsdorff, 1995; Ulmer et al., 1994). In some experiments (V1152, ES372, ES369, V1155, and V1210) antigorite appeared to remain stable above its predicted dehydration temperature (Figure 3). Most of these experiments were run at 700°C for only 1, 6, or 24 hr, respectively. The temperature overstep for the antigorite dehydration reaction in these experiments is in the range of 50°C–70°C and the reaction kinetics are expected to be slow. Our experiments indicate that at least 48 hr are required for complete dehydration at 700°C (cf. experiment V1189). However, <1 hr is sufficient at 800°C (cf. experiment

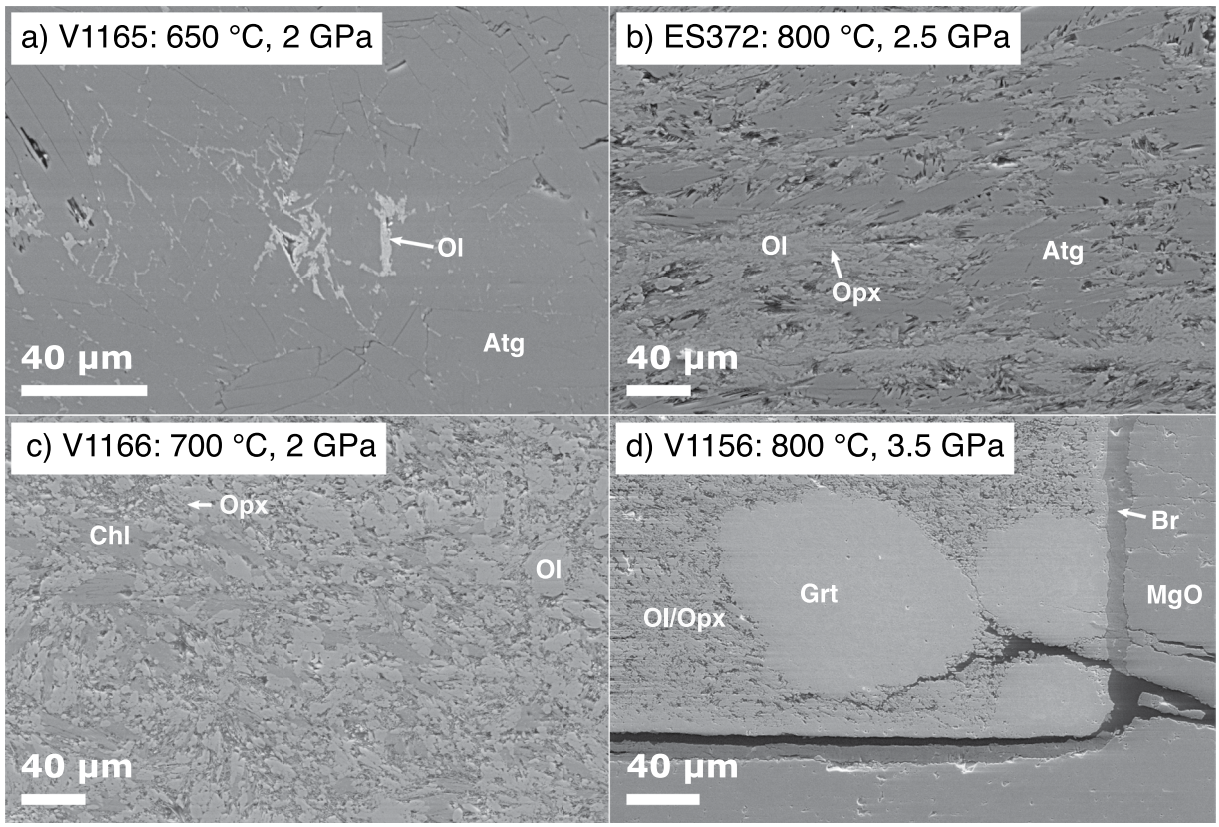

Figure 2. (a) The onset of antigorite dehydration is marked by the formation of Fe-rich olivine along the grain boundaries. (b) Olivine and orthopyroxene grow to large patches between antigorite crystals. Note the high temperature in experiment ES372, indicating metastability of antigorite (see also explanations in main text). (c) Antigorite reacts to chlorite, while the patchy texture (Figure 2b) is preserved. (d) At high temperatures and pressures garnets with a poikiloblastic texture are observed.

ES367). The presence of antigorite in experiment ES372, run at 800°C for 0.5 hr (the same nominal conditions as ES367) thus likely arises from a slightly overestimated temperature. Nevertheless, due to the reliability and extensive use of this type of graphite heater assembly at the BGI uncertainties in temperature estimation are expected to be within 50°C.

Antigorite in the run products has an Al_2O_3 content of 2.6(2) wt% and an Mg# (molar MgO/(MgO + FeO), with FeO being total Fe as FeO) of 0.94(1), similar to the starting material. Chlorite has generally a higher Mg# with respect to Atg of 0.96(2) and a temperature-dependent Al_2O_3 content. Sample V1170 run at 500°C, using SETUP II, shows the formation of a 100 µm thick layer of chlorite as a result of interaction between the antigorite and Al_2O_3 layers. This chlorite has a significantly higher Al_2O_3 content of 21.2 wt% due to interaction with the Al-rich fluid source. The Mg# of olivine in the run products is 0.93(2), whereas a layer of olivine that formed through interaction between the drill core and the MgO sleeve has a higher Mg# of about 0.96(1). Orthopyroxene coexisting with olivine has a slightly higher Mg#. The Mg-Fe exchange between newly formed olivine and orthopyroxene appears to reach equilibrium as it is in agreement with experimental data from von Seckendorff & O'Neill (1993).

Figure 4 summarizes the EBSD results of samples V1152 and V1156. Both samples were drilled perpendicular to the macroscopic preferred orientation of antigorite (Table 1) and we assume that the initial antigorite preferred orientation was similar prior to the experiment. Sample V1152 did not show any dehydration products and preserved this initial texture of serpentine, assuming no recrystallization took place. The two areas mapped consist mainly of antigorite and magnetite and show that the indexing rate of the antigorite was 80%–90% (Figure 4a). The pole figures of antigorite confirm a strong preferred orientation (Figures 4c and 4d). The antigorite platelets show a crystallographic-preferred orientation with the *c* axis at an angle of ~45° oblique to the drill core axis. At elevated temperature experiment V1156 consists of olivine, orthopyroxene, and garnet (Figure 4b). All phases, including the brucite-layer and the MgO sleeve could be indexed in the EBSD measurements. The two mapped

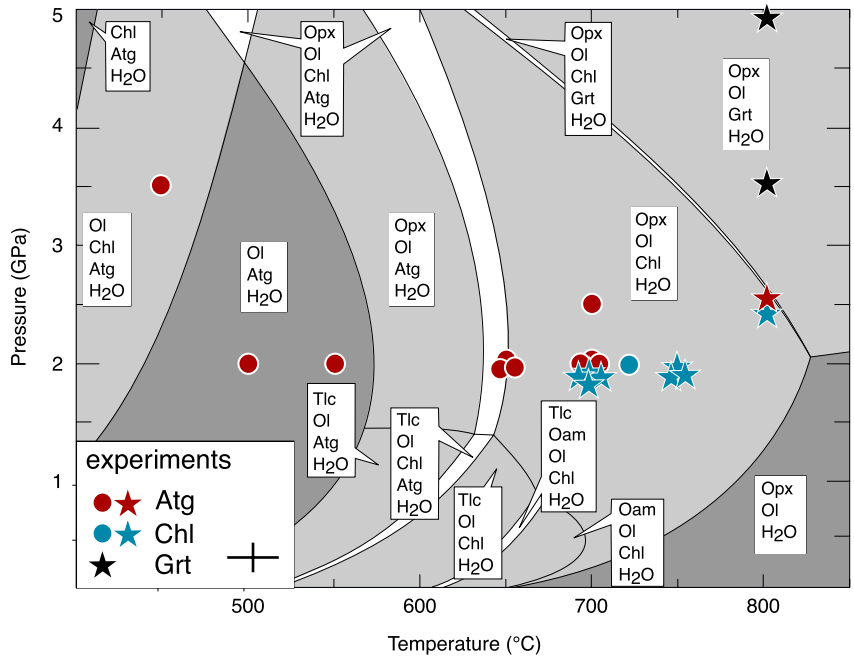

Figure 3. Pseudosection calculated with Perple_X for the composition SiO_2 = 42.81 wt%, Al_2O_3 = 2.04 wt%, FeO = 4.49 wt%, MgO = 38.43 wt%, and H_2O = 12.23 wt% (version 6.8.1, HP11 database and CORK EoS for fluids). The composition was changed with respect to the starting material composition (Table A-2 in Supporting Information S1) in order to match the observed phase modes in run products. Stars mark experiments used to determine the fluid flux. Circles mark experiments without fluid-induced brucite formation. The black cross indicates a conservative standard error of 30°C and 0.25 GPa.

areas indicate that olivine has a preferred orientation direction related to the precursor antigorite (Figure 4e), assuming the latter was similar to antigorite in V1152. Brucite has a slightly stronger preferred orientation than olivine and is aligned with the *c* axis parallel to the contact with the drill core (Figure 4f).

3.2. Brucite Formation

Brucite layers were formed in the MgO surrounding the serpentine drill core in all experiments run at temperatures above 550°C, whereas at lower temperatures antigorite and MgO did not react (Figure 5a). Adjacent to the brucite layer surrounding the drill core an additional olivine layer formed within the drill core (Figures 5b–5d). It is important to note that these double layers already start to form below the antigorite dehydration temperature. In these experiments the brucite layer is found to be thinner than the olivine layer (Figure 5b). On the other hand, in experiments showing evidence for partial or complete dehydration, that is, the presence of olivine + orthopyroxene ± garnet, the brucite layer is significantly thicker with respect to the adjacent olivine layer (Figures 5c and 5d). A full list of brucite and olivine layer thicknesses can be found in the Text A-3 in Table S1.

The thicknesses of both brucite and olivine layers are also strongly time-dependent (Figure 6). The largest increase in layer thickness is observed within the first 24 hr. Below the dehydration temperature the maximum thickness of the brucite layer, 5–10 μm, is reached within these 24 hr. In experiments exceeding the dehydration temperature significantly more brucite is formed. A maximum thickness of 30–40 μm is also reached after ≈72 hr at 700°C. The data indicate that at higher temperatures the maximum is reached already after 24 hr. The brucite layer is always thicker in the radial direction of the drill core axis with respect to the axial direction, regardless of the orientation of the serpentine foliation with respect to the drill core axis.

The fluid flux through antigorite prior to dehydration was probed in experiment V1170 (Figure 7) using SETUP II and an $Al(OH)_3$ fluid source. Although antigorite did not start to dehydrate in this experiment, chlorite is observed at the bottom of the drill core (Figure 7c) resulting from reaction with the fluid source. Quantitative SEM analyses on the $Al(OH)_3$ dehydration product shows it to be corundum. Previous experimental and

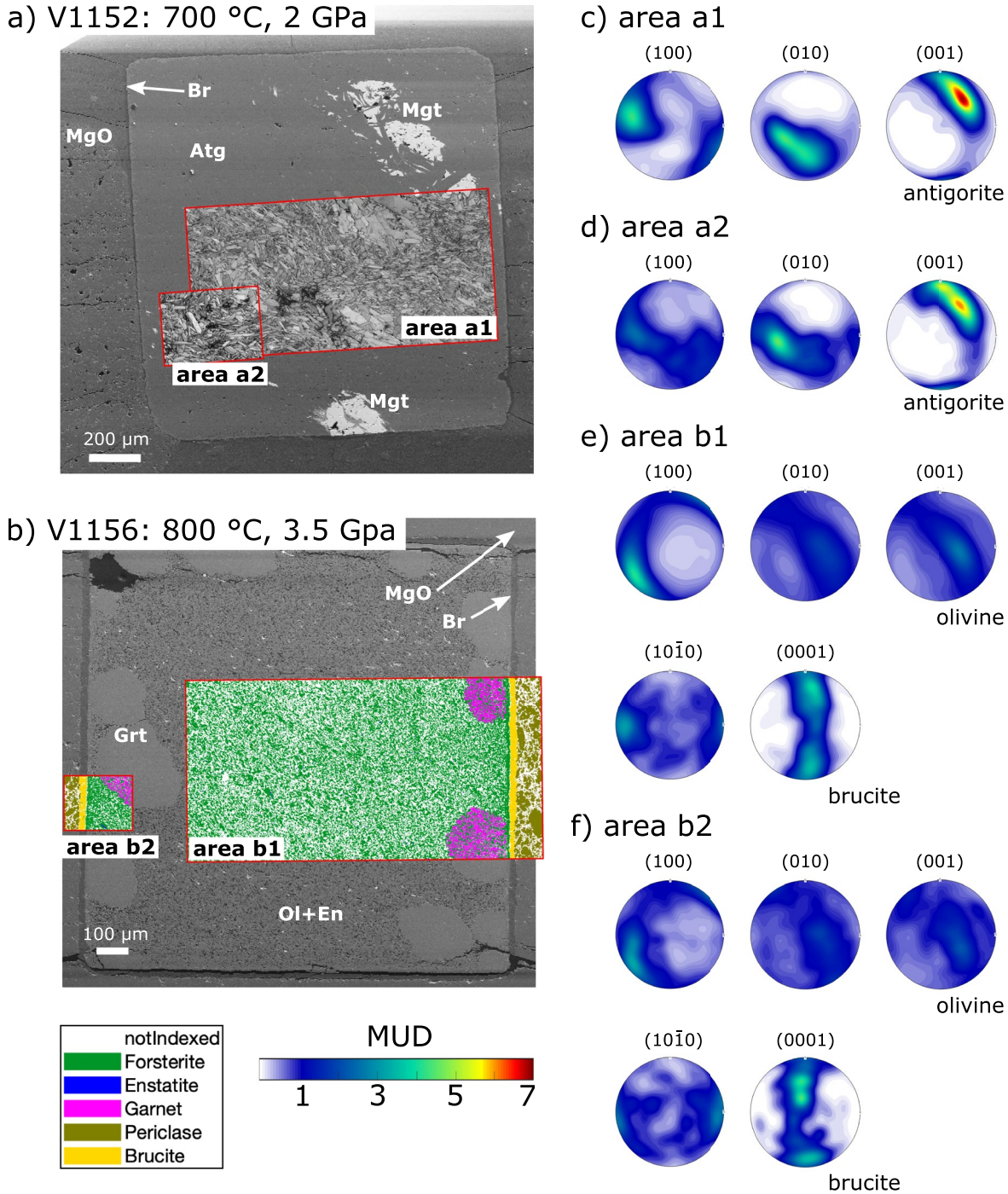

Figure 4. Electron backscattered diffraction measurements. (a) Sample V1152 consists of antigorite with magnetite. Two areas were mapped and indicated with the band contrast. (b) Sample V1156 represents a completely dehydrated serpentinite. All phases could be indexed, including the brucite layer and the MgO sleeve. (c–d) Polefigures (lower hemisphere) of antigorite in the two areas shown in (a), colored for multiples of uniform distribution (MUD). (e, f) Polefigures (lower hemisphere) of olivine and brucite of the two areas shown in Figure 4b.

thermodynamic studies predict the formation of corundum at 2 GPa and 550°C (Fockenberg et al., 1996; Grevel et al., 2000), which probably implies a slight underestimate of the run temperature of 500°C. In experiment V1170 a thin double layer of olivine and brucite formed at the top of the drill core, similar to what is observed in the other experiments. Nonetheless, the majority of brucite formed at the junctions between the antigorite, MgO and

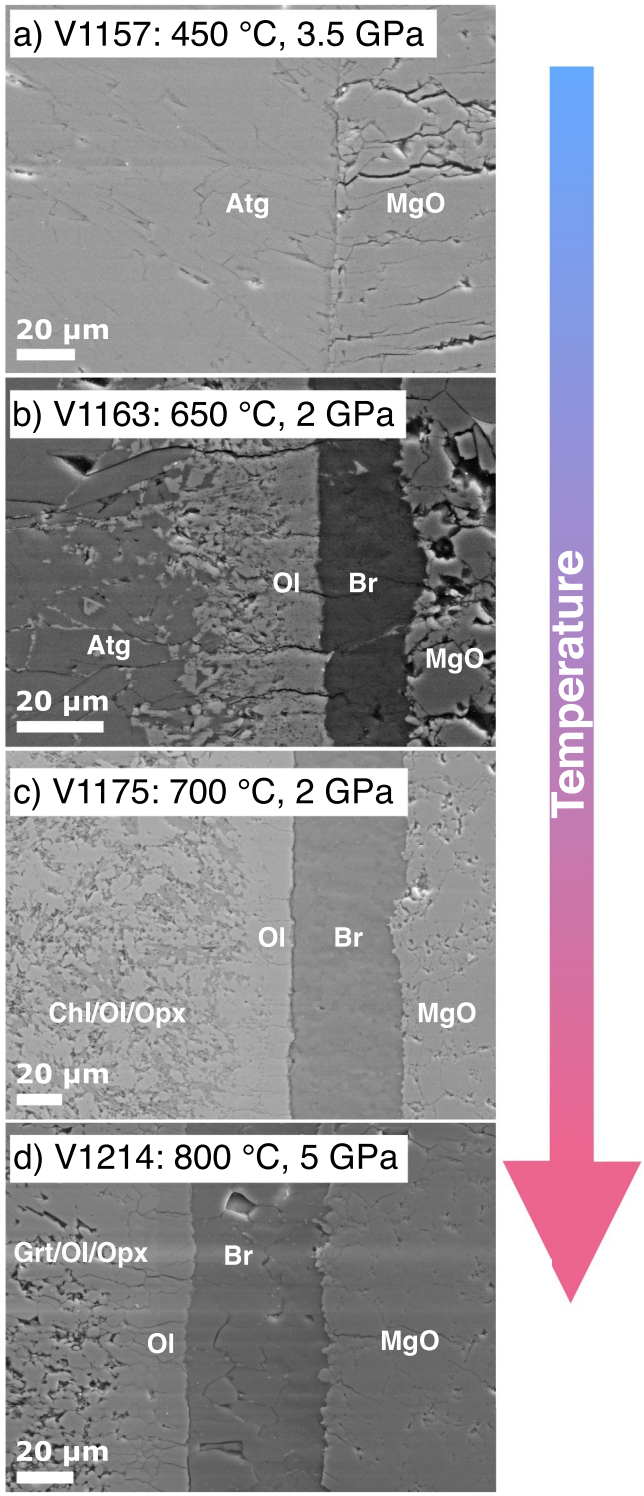

Figure 5. Evolution of the brucite layer as a function of temperature. The right side of the serpentine drill core is shown (the dark blue rectangle in Figure 1a). (a) At low temperatures no reaction is observed. (b) A double layer of brucite and olivine forms at temperatures where antigorite is still stable. The brucite layer is thinner with respect to the olivine layer. (c) As soon as antigorite dehydrates, the brucite layer grows thicker than the adjacent olivine layer. (d) An anomalously thin brucite layer formed at elevated pressure. The grain size within the brucite layer reaches up to 20 µm.

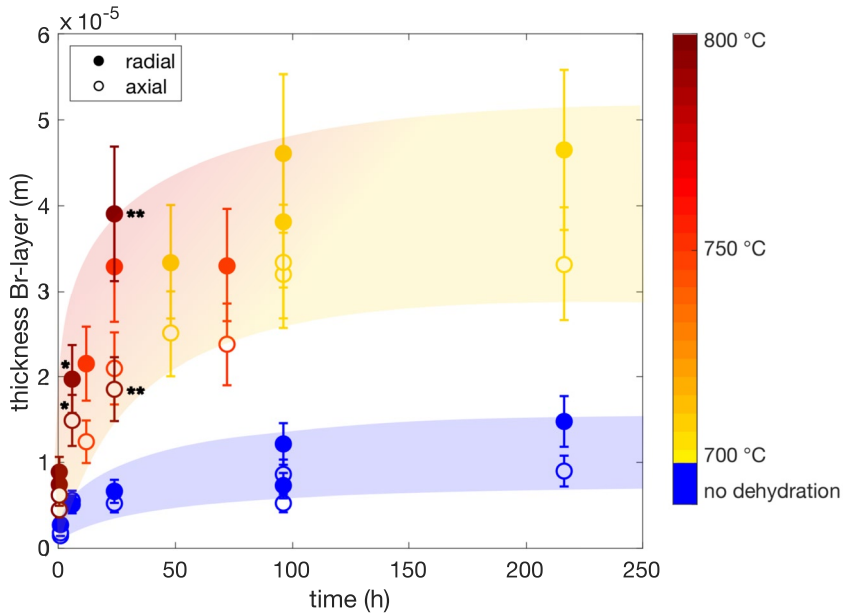

Figure 6. The brucite layer thickness as a function of experimental run time. Blue symbols show the thickness of brucite layers formed in experiments at temperatures or time scales below antigorite dehydration. Warm colors indicate the brucite layer thickness in experiments above the antigorite dehydration temperature, color coded for temperature. It can be observed that the brucite layer growth ceases after 72 hr at 700°C and after 24 hr at 750°C. * marks experiment V1156 (3.5 GPa) and ** marks experiment V1214 (5 GPa). The brucite layer is always thicker in the radial direction compared to the axial direction.

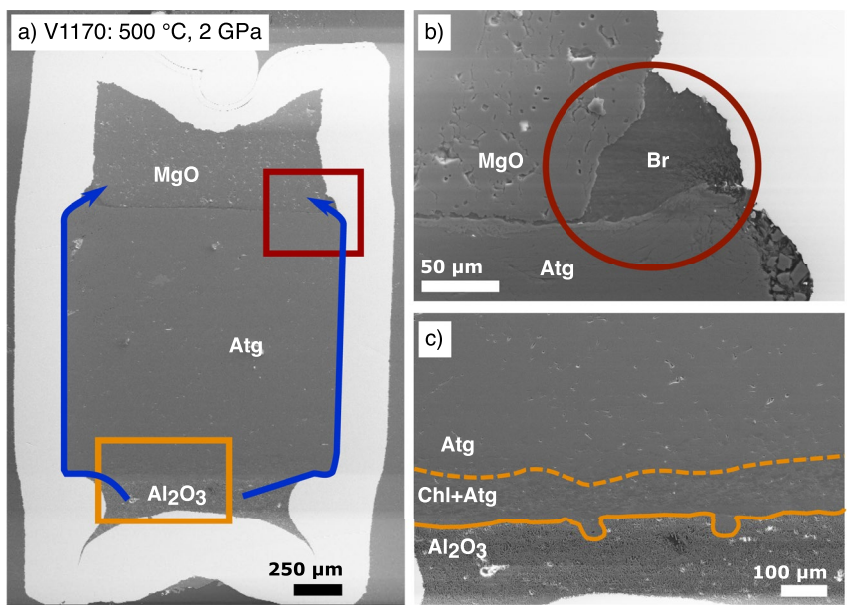

Figure 7. (a) Experiment V1170 used to probe the fluid flux through antigorite prior to dehydration. SETUP II (Figure 1b) is used with a fluid source at the bottom and a fluid sink on top of the serpentinite drill core. Rectangles mark the positions of subfigures (b) (red) and (c) (orange), showing details of the top and bottom. Blue arrows mark the fluid flow path as described in the main text. (b) On top of the drill core a region of brucite formed at the triple junction antigorite-MgO-capsule. (c) A chlorite-ric layer formed from the interaction between the Al-rich fluid source and antigorite.

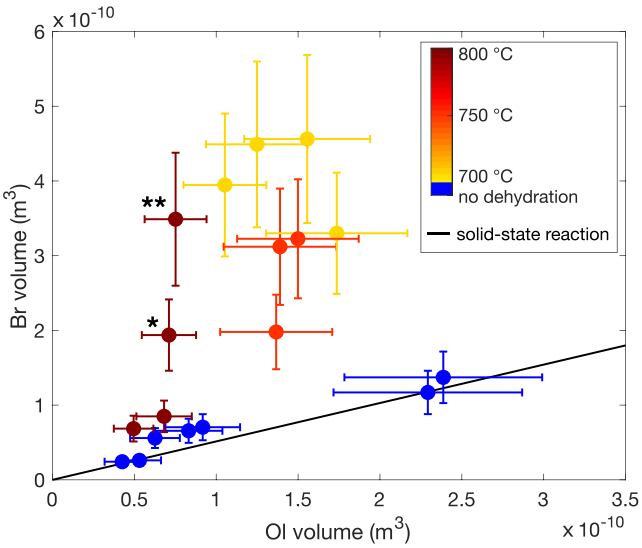

Figure 8. The volume of olivine versus brucite monomineralic layers in experimental run products. Prior to antigorite dehydration (blue symbols) the volume ratio between the two monomineralic layers is 0.5144, as predicted by the solid reaction (Equation 7). The brucite layer in experiments showing prominent dehydration (yellow to red symbols) exceeds this ratio. * marks experiment V1156 (3.5 GPa) and ** marks experiment V1214 (5 GPa).

AuPd capsule (Figure 7b). This observation indicates that the fluid migrated only along the capsule-antigorite interface, as indicated in Figure 7a, rather than through the drill core.

4. Discussion

The objective of the experiments is to investigate the fluid flux at high *PT* conditions. Using Equations 1 and 2, we then can estimate diffusivities and permeabilities. However, in our specific system reactions between the serpentinite and the surrounding MgO, serving as a fluid sink, formed an additional double layer of olivine and brucite. It is first necessary to understand differences in the formation mechanisms of this double layer at temperatures below and above serpentine dehydration and how this influences the determined fluid flux. Furthermore, µCT-scans have been performed to show changes in pore space due to fluid flux. The findings are then used to discuss the fluid flux in hydrated lithospheric mantle within subduction zones and also with respect to the potential brittle failure of subducted serpentinites.

4.1. Brucite Formation Mechanism

In all experiments performed at temperatures >500°C, a brucite layer formed around the drill core adjacent to an inner monomineralic layer of olivine (Figure 5). These double layers even formed at temperatures below antigorite dehydration (Equation 4). Brucite formation can thus be divided into a solid-state reaction that also occurs prior to dehydration and a fluid-induced reaction at temperatures exceeding dehydration (Equation 4) (Figure 1c). The solid-state reaction is

$$\text{antigorite} + 51\,\text{MgO} = 34\,\text{olivine} + 31\,\text{brucite}. \tag{7}$$

This reaction does not involve a free fluid phase. Thus, the growth of brucite from this reaction does not record a fluid flux. The thickness of the olivine layer, which has a higher Mg# compared to olivine formed through antigorite dehydration, provides an indication of how much brucite has been formed through this solid-state reaction. In reaction (Equation 7) brucite and olivine are formed in the molar ratio 31:34. Using the molar volumes for brucite and olivine of 24.63 and 43.66 cm^3/mol (Holland & Powell, 2011), respectively, we obtain a volume ratio of 0.5144. The volumes of each phase formed during the experiments can be calculated directly from layer thicknesses. The total volume of brucite is given as

$$V_{\text{brucite}} = V_{\text{radial}} + V_{\text{axial}}, \tag{8}$$

with V_{radial} and V_{axial} being the volume of brucite formed in radial and axial direction given by

$$V_{\text{radial}} = \left[(r + d_{\text{radial}})^2 - r^2\right] \pi\, h \tag{9}$$

$$V_{\text{axial}} = 2\, r^2\, \pi\, d_{\text{axial}}, \tag{10}$$

with r and h being the radius and the height of the drill core, respectively, and d is the thickness of the brucite layer in the axial or radial direction. The calculation for the volume of the monomineralic olivine layer is similar, although it must be considered that the layer formed inside the drill core.

Figure 8 shows the measured volumes of olivine versus brucite in each experiment. Indeed, experiments not showing prominent antigorite dehydration (blue symbols) fall onto the expected stoichiometric ratio from solid-state reaction (Equation 7) indicating that only solid-state brucite formation occurred. In experiments where dehydration of antigorite occurs (yellow to red symbols), the brucite layer is thicker than expected from the solid-state reaction alone. The fluid produced in the dehydration reactions (Equations 4 and 5) thus migrated toward the MgO sleeve where hydration (Equation 6) results in additional growth of the brucite layer.

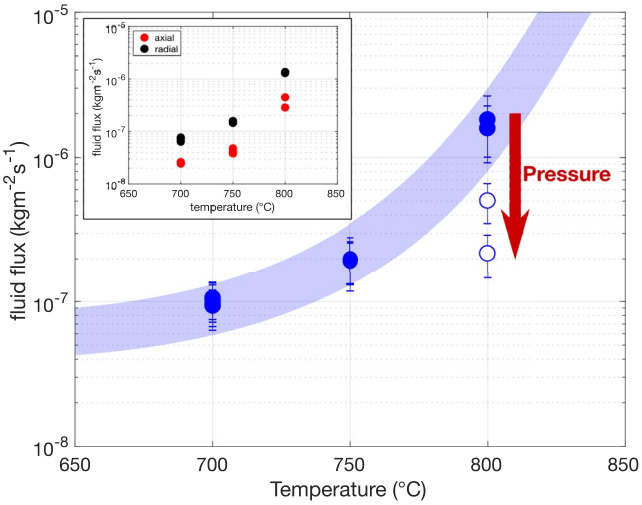

Figure 9. The experimental fluid flux calculated as a function of temperature. The time period over which fluid flows out of the cylinder is shorter than the run time in long duration experiments. We used a temperature-dependent maximum time to calculate the fluid flux as explained in the main text. Open symbols mark experiments performed at 3.5 and 5 GPa. The inset shows the fluid flux in the axial and radial directions for experiments performed at 2 and 2.5 GPa (filled symbols in main figure), indicating a slightly larger fluid flux in the radial direction.

4.2. Fluid Flux Determination

The mean fluid flux q, that is, the mass of fluid discharged per time and area, is given as

$$q = m_{\text{fluid}} / \left[A\, t^{*} \right], \tag{11}$$

where m_{fluid} is the mass of fluid stored in the brucite layer, A is the surface area of the drill core, and t^{*} is the time over which the fluid flux is active. Since a brucite volume corresponding to 0.5144 V_{Ol} results from the solid-state reaction (Equation 7), V_{Br} has to be corrected for this solid-state contribution to obtain the volume of brucite V^{*}_{Br} that effectively results from the discharge of a free fluid. m_{fluid} is determined from V^{*}_{Br} using the H_2O mass fraction in brucite $X = 0.309$ and the density of brucite $\rho_{\text{Br}} = 2{,}370$ kg/m^3:

$$m_{\text{fluid}} = X\, V^{*}_{\text{Br}}\, \rho_{\text{Br}}. \tag{12}$$

The release of fluid decreases over time and then finally ceases as observed in long duration experiments (Figure 6). The mean fluid flux calculated for longer experiments is thus expected to be smaller with respect to short experiments. However, if the fluid flux ceases during the experiment, the mean fluid flux is considerably underestimated by using the total run time in Equation 11. Assuming experiments that run sufficiently long (>12 hr) at similar conditions will result in a similar mean fluid flux, we can estimate the time t^{*} of active fluid flux, by minimizing the difference in the calculated fluid flux at fixed temperature. Estimated t^{*} is 72 hr for 700°C experiments and 24 hr for experiments at ≥750°C. These values are also in agreement with results from Figure 6. Consequently, all experiments with $t > t^{*}$, have to be restricted to t^{*}.

Figure 9 shows that the fluid flux increases by almost two orders of magnitude from 700°C to 800°C in partially dehydrated experiments conducted at 2–2.5 GPa. Completely dehydrated experiments V1156 (3.5 GPa) and V1214 (5 GPa), conducted at 800°C, show a gradual decrease in the fluid flux with increasing pressure. A slightly larger fluid flux is observed in the radial direction with respect to the axial direction, that is, direction of the thermocouple, in all experiments. Since this observation is independent of the orientation between the drill core axis and the serpentine foliation direction, we interpret this to result from a small deviatoric stress in the axial direction, likely resulting from the use of a relatively hard alumina thermocouple tube.

4.3. Fluid Transport Processes

The partially and completely dehydrated serpentinite samples do show a high porosity (Figures 2, 4 and 5). µCT-scans on the recovered samples indicate a porosity of >20% and a high connectivity of the pore space. In such a texture the fluid can be expected to be transported via a darcian fluid flow. Although thin (3–26 µm), the olivine layer is compact and does not show a high porosity (Figure 5). In this very dense layer diffusion is the expected transport mechanism. To interpret the experimental results it is important to consider both the fluid flux through the permeable partially to completely dehydrated serpentinite and diffusion through the olivine layer (see Text B-3 in Supporting Information S2 for an additional experiment demonstrating that the brucite layer does not limit the fluid flux).

The calculation of the permeability in serpentinites is derived from the fluid pressure upon dehydration reaction (compare Text B-1 in Supporting Information S2 for detailed description). However, permeabilities calculated for our experiments are far below the percolation threshold, despite the highly connected pore space. Potential error sources include the calculation of the fluid pressure as well as neglecting pressure imposed from the newly formed brucite layer onto the cylinder. This latter effect could decrease the pressure gradient across the sample. Furthermore, elastic behavior of the assembly could also decrease the pressure gradient and thus cause an underestimation of the permeability. It is also possible that the pore space is less connected than assumed. Small pores and small pore throat diameters, that might not be resolved in µCT-scans, combined with a high tortuosity, could

cause an overestimated connectivity. However, it is also likely that the fluid flux is mainly controlled by the slower diffusion process. This is further supported by experiment V1214, performed at 5 GPa. In this sample a brucite layer formed despite the fluid underpressure at these conditions. We can, however, not exclude that the positive excess pressure up to 600 MPa in most experiments affects the fluid transport.

To examine fluid diffusion through the olivine layer we obtain the concentration gradient from the amount of fluid produced within the serpentine (compare Text B-1 in Supporting Information S2). The calculated diffusion constants of H_2O in olivine are in the range 6.8×10^{-13}–1.4×10^{-12} m^2/s. Demouchy (2010) obtained a diffusion constant for hydrogen in olivine, which is significantly higher with respect to the data obtained here, although it must be considered that our experiments employed higher pressures. Furthermore, the MgO hydration results in a positive volume change, so that the newly formed brucite may impose stress on the olivine layer and further decrease grain boundary width.

Finally an estimate on the fluid flux through serpentinite prior to dehydration can be determined from experiment V1170 (500°C, 2 GPa), which employed an $Al(OH)_3$ fluid source. Since in experiment V1170 only a minor fluid flow between the serpentinite and the capsule wall was observed, it seems that serpentine prior to the onset of dehydration is quite impermeable. However, we can estimate an upper limit for the fluid flux by assuming that the sample was on the verge of producing a brucite layer of infinitesimal thickness. Considering a high pressure porosity of 4×10^{-6} (Kawano et al., 2011) the total water volume in the serpentinite sums up to 1.06×10^{-14} m^3. Within 96 hr of run time this amount of fluid passed through the bottom area A, giving rise to a fluid flux of 1.74×10^{-11} $kg/(m^2\ s)$. The fluid pressure gradient through the capsule can be estimated from the dehydration of gibbsite to corundum:

$$2\ Al(OH)_3 \rightarrow Al_2O_3 + 3\ H_2O. \quad (13)$$

The bulk modulus of gibbsite is given as 49 GPa (Liu et al., 2004). The thermal volume expansion coefficient determined from the data of Mercury et al. (2006) is 5.5×10^{-5} K^{-1}. Using data for corundum from Holland and Powell (2011), the solid volume change in reaction (13) based on the modified tait EoS is -42 cm^3. This corresponds to a molar fluid density of 0.07 mol/cm^3, which yields an overpressure on dehydration of 1.0 GPa. Using the same approach of transforming a pressure gradient into a concentration gradient as explained in B-1 in Supporting Information S2, we obtain a diffusion coefficient for serpentine of 1×10^{-16} to 5×10^{-17} $m^2\ s^{-1}$, significantly lower with respect to olivine. A porosity change of one order of magnitude causes a change in diffusivity of the same order. However, as the porosity of rocks under the experimental conditions likely tends toward zero (Plümper, Botan, et al., 2017; Plümper, John, et al., 2017), the value employed is quite conservative.

4.4. µCT-Scans

µCT analyses and flow simulation were performed on two samples (ES367 and V1167) using the software GeoDict, version 2,021. For segmentation of the data Otsu's method (Otsu, 1979) was used. More detail on data reduction can be found in the Text B-2 in Supporting Information S2. Sample ES367 yields a total porosity of 22%, whereas the porosity in experiment V1167 is higher with 33%. Mass balance indicates 5 wt% chlorite in sample ES367, whereas about 13 wt% fluid is released. In sample V1167 the remaining chlorite mass is higher with approximately 12 wt% but the released fluid mass is similar with 12 wt%. Consequently, any difference in porosity, given a similar progress in dehydration, is caused by the loss of fluid and subsequent compaction. In experiment V1167 all fluid remained in the drill core because the serpentinite sample was welded, without surrounding materials, into an AuPd capsule. The amount of brucite formed in experiment ES367, however, shows that about 30% of the total fluid was lost to the MgO sleeve and is thus in very good agreement with a porosity reduction by 33% as obtained from the µCT-scans.

The permeability at room *PT* conditions determined from µCT scans is of the order of 10^{-15} m^2. This value is significantly higher with respect to the permeabilities calculated for high *PT* conditions (Table A-4 in Supporting Information S1), and slightly higher with respect to permeabilities obtained by Ganzhorn et al. (2019) extrapolated to room pressure. This indicates that partially dehydrated serpentinites indeed have a higher permeability than pure serpentinites, in agreement with the study by Tenthorey and Cox (2003).

4.5. Influence of Serpentine Dehydration on Subduction Zone Fluid Flux

Intermediate-depth earthquakes appear to be organized in a double seismic zone, where the seismicity is thought to be thermally activated and may be, particularly in the lower seismic zone, related to the dehydration of serpentine (Ferrand et al., 2017; Jung et al., 2004). Several studies that have analyzed dehydration kinetics have shown that the dehydration of antigorite has a fluid production rate of the order of 10^{-4} to 10^{-8} $m^3_{\text{fluid}} / \left(m^3_{\text{rock}} \text{s}\right)$ (Chollet et al., 2011; Perrillat et al., 2005), similar to the fluid production rate for brucite dehydroxylation (Liu et al., 2017). This rate is found to be significantly faster with respect to the relaxation time of the solid rock and hence, brittle fracturing is likely to occur (Schwartz et al., 2001).

We could not determine the fluid flux through partially dehydrated serpentinites due to the formation of an olivine layer. However, we could determine the fluid flux through olivine and give an upper estimate of fluid flux through serpentine prior to dehydration. The fluid flux in serpentinites at conditions of brucite dehydration (Equation 3) is extremely low in the order of 10^{-14} $m^3/(m^2\ s)$. Thus, a large fluid overpressure can build up during brucite dehydration and might cause brittle failure of the rock.

When the serpentinites dehydrate (Equations 4 and 5) a large open pore space forms. Since the pore space is highly connected, as shown by our μCT-scans, and percolation is expected to be fast, the fluids are likely to dissipate. However, the oceanic lithosphere is often only partially serpentinized and it is not uncommon to find fresh peridotites in the vicinity of serpentinites. If the serpentinite is adjacent to a unaltered peridotite, the fluid cannot escape fast enough through percolation due to the large fluid production rate, similar to our experiments in which the fluid flux is inhibited by the surrounding olivine layer. Consequently, even if a connected pore space evolves, an adjacent low permeable lithology has the potential to inhibit the fluid flux and brittle fracturing may occur due to fluid pressure build up at conditions of positive volume change.

5. Conclusions

We have developed a new experimental method that enables fluid flux to be determined at high *PT* conditions. The method uses the dehydration of a fluid source, both external and internal, and formation of hydrous minerals in the fluid sink to immobilize the migrating fluids. Combined with estimates of pore fluid pressure, this method can be used to place constraints on mineral and rock permeabilities or diffusivities.

The technique is used here to study the fluid flux during dehydration of serpentinite where the serpentinite itself provides the fluid source (SETUP I). Fluid flowing into MgO surrounding the serpentinite drill core produces brucite and the volume of brucite in the recovered experiments provides an estimate for the volume of fluid that has flown out of the drill core. A correction must be made for a small volume of brucite formed through a solid-state reaction, which also creates a dense olivine layer. With an additional experiment we could show that the formation of brucite does not limit the fluid flux into the unreacted MgO. However, the dense olivine layer lowers the fluid flux into the MgO. μCT-scans performed to analyze the pore space, showed that fluid flux within the partially dehydrated serpentinite is expected to be significantly higher with respect to the observed fluid flux in our experiments. Consequently, fluid flux within subduction zones can be high at dehydration conditions, if the fluid is not bound by an adjacent impermeable lithology.

We also performed experiments with an external fluid source (SETUP II), which can be used to study fluid flow at conditions prior to dehydration or also through dry samples. Careful analyses of the run products revealed that the fluid likely migrated around the sample and thus only allows for an upper estimate of the fluid flux of 1.74×10^{-11} $kg/(m^2\ s)$. Our results show that serpentinites are an impermeable layer within subduction zones. As a consequence, small amounts of fluid released early within serpentinites, that is, through dehydration of brucite, will result in fluids trapped in the serpentinite. This can result in considerable overpressures.

The experimentally determined fluid flux was found to differ slightly between axial and radial directions, although this was found to not be influenced by the orientation of the serpentinite foliation. This difference most likely arises from a small differential stress in the axial direction of the multianvil assembly. This highlights the important influence of deformation on fluid flow. Deformation modifies the local stress distribution, the development of preferred orientation and can additionally open or close existing pore space. Extensive shear deformation in subduction zones could have an effect on the fluid flux if it persists during dehydration.

Conflict of Interest

The authors declare no conflicts of interest relevant to this study.

Data Availability Statement

All data used in this work are available as supporting information. The μCT-scans can be found in the data repository https://doi.org/10.24416/UU01-PB440D.

Acknowledgments
We thank José Alberto Padrón-Navarta, two anonymous reviewers, and Editor Whitney Behr for their constructive comments that helped to improve the manuscript considerably. Hubert Schulze, Raphael Njul, and Alexander Rother are thanked for excellent sample preparation and Florian Heidelbach for the help with EBSD measurements. We thank Elias Kempf for providing the foliated antigorite-serpentinite sample. The X-ray tomography experiments were performed at SPring-8 with the approval of the Japan Synchrotron Radiation Research Institute (JASRI) (Proposal nos. 2018A1471 and 2019B1785). This study was financed by the international research and training group Deep Earth Volatile Cycles DFG Grant No. GRK 2156/1 and partly supported by JSPS Japanese-German Graduate Externship, DFG Grant Nos. FR1555/11, DFG Grant Nos. TH2076/8-1, and the NWO Grant No. VI.Vidi.193.030. Open Access funding enabled and organized by Projekt DEAL.

References

Arnulf, A. F., Bassett, D., Harding, A. J., Kodaira, S., Nakanishi, A., & Moore, G. (2022). Upper-plate controls on subduction zone geometry, hydration and earthquake behaviour. *Nature Geoscience*, *15*(2), 143–148. https://doi.org/10.1038/s41561-021-00879-x

Bachmann, F., Hielscher, R., & Schaeben, H. (2010). Texture analysis with MTEX-free and open source software toolbox. In *Solid state phenomena* (Vol. 160, pp. 63–68). Trans Tech Publications Limited. https://doi.org/10.4028/www.scientific.net/SSP.160.63

Becker, J., Biebl, F., Cheng, L., Glatt, E., Grießer, A., Groß, M., et al. (2020). *Geodict software*. Math2Market GmbH.

Bose, K., & Ganguly, J. (1995). Quartz-coesite transition revisited: Reversed experimental determination at 500–1200°C and retrieved thermochemical properties. *American Mineralogist*, *80*(3–4), 231–238. https://doi.org/10.2138/am-1995-3-404

Bromiley, G. D., & Pawley, A. R. (2003). The stability of antigorite in the system MgO-SiO_2-H_2O (MSH) and MgO-Al_2O_3-SiO_2-H_2O (MASH): The effects of Al^{3+} substitution on high-pressure stability. *American Mineralogist*, *88*(1), 99–108. https://doi.org/10.2138/am-2003-0113

Cai, C., Wiens, D. A., Shen, W., & Eimer, M. (2018). Water input into the Mariana subduction zone estimated from ocean-bottom seismic data. *Nature*, *563*(7731), 389–392. https://doi.org/10.1038/s41586-018-0655-4

Chollet, M., Daniel, I., Koga, K. T., Morard, G., & van de Moortle, B. (2011). Kinetics and mechanism of antigorite dehydration: Implications for subduction zone seismicity. *Journal of Geophysical Research*, *116*(4), 1–9. https://doi.org/10.1029/2010JB007739

Demouchy, S. (2010). Diffusion of hydrogen in olivine grain boundaries and implications for the survival of water-rich zones in the Earth's mantle. *Earth and Planetary Science Letters*, *295*(1–2), 305–313. https://doi.org/10.1016/j.epsl.2010.04.019

Faccenda, M., Gerya, T. V., & Burlini, L. (2009). Deep slab hydration induced by bending-related variations in tectonic pressure. *Nature Geoscience*, *2*(11), 790–793. https://doi.org/10.1038/ngeo656

Ferrand, T. P., Hilairet, N., Incel, S., Deldicque, D., Labrousse, L., Gasc, J., et al. (2017). Dehydration-driven stress transfer triggers intermediate-depth earthquakes. *Nature Communications*, *8*(1), 15247. https://doi.org/10.1038/ncomms15247

Fockenberg, T., Wunder, B., Grevel, K.-D., & Burchard, M. (1996). The equilibrium diaspore-corundum at high pressures. *European Journal of Mineralogy*, *8*(6), 1293–1299. https://doi.org/10.1127/ejm/8/6/1293

Fusseis, F., Schrank, C., Liu, J., Karrech, A., Llana-Fúnez, S., Xiao, X., & Regenauer-Lieb, K. (2012). Pore formation during dehydration of a polycrystalline gypsum sample observed and quantified in a time-series synchrotron X-ray micro-tomography experiment. *Solid Earth*, *3*(1), 71–86. https://doi.org/10.5194/se-3-71-2012

Ganzhorn, A. C., Pilorgé, H., & Reynard, B. (2019). Porosity of metamorphic rocks and fluid migration within subduction interfaces. *Earth and Planetary Science Letters*, *522*, 107–117. https://doi.org/10.1016/j.epsl.2019.06.030

Gorman, P. J., Kerrick, D. M., & Connolly, J. A. D. (2006). Modeling open system metamorphic decarbonation of subducting slabs. *Geochemistry, Geophysics, Geosystems*, *7*(4), Q04007. https://doi.org/10.1029/2005GC001125

Grevel, K.-D., Burchard, M., & Faßhauer, D. W. (2000). Pressure-volume-temperature behaviour of diaspore and corundum: An in situ X-ray diffraction study comparing different pressure media. *Journal of Geophysical Research*, *105*, 27877–27887.

Grove, T. L., Chatterjee, N., Parman, S. W., & Médard, E. (2006). The influence of H_2O on mantle wedge melting. *Earth and Planetary Science Letters*, *249*(1–2), 74–89. https://doi.org/10.1016/j.epsl.2006.06.043

Holland, T. J. B., & Powell, R. (2011). An improved and extended internally consistent thermodynamic dataset for phases of petrological interest, involving a new equation of state for solids. *Journal of Metamorphic Geology*, *29*(3), 333–383. https://doi.org/10.1111/j.1525-1314.2010.00923.x

Huang, Y., Nakatani, T., Nakamura, M., & McCammon, C. (2019). Saline aqueous fluid circulation in mantle wedge inferred from olivine wetting properties. *Nature Communications*, *10*(1), 5557. https://doi.org/10.1038/s41467-019-13513-7

Huang, Y., Nakatani, T., Nakamura, M., & McCammon, C. (2020). Experimental constraint on grain-scale fluid connectivity in subduction zones. *Earth and Planetary Science Letters*, *552*(October), 116610. https://doi.org/10.1016/j.epsl.2020.116610

Johnson, M. C., & Walker, D. (1993). Brucite [Mg(OH)2] dehydration and the molar volume of H_2O to 15 GPa. *American Mineralogist*, *78*, 271–284.

Jung, H., Ii, H. W. G., & Dobrzhinetskaya, L. F. (2004). Intermediate-depth earthquake faulting by dehydration embrittlement with negative volume change. *Nature*, *428*(6982), 545–549. https://doi.org/10.1038/nature02412

Kawano, S., Katayama, I., & Okazaki, K. (2011). Permeability anisotropy of serpentinite and fluid pathways in a subduction zone. *Geology*, *39*(10), 939–942. https://doi.org/10.1130/G32173.1

Kelemen, P. B., & Manning, C. E. (2015). Reevaluating carbon fluxes in subduction zones, what goes down, mostly comes up. *Proceedings of the National Academy of Sciences*, *112*(30), E3997–E4006. https://doi.org/10.1073/pnas.1507889112

Keppler, H., & Frost, D. J. (2005). Introduction to minerals under extreme conditions. *Mineral Behaviour at Extreme Conditions*, *6*, 1–30. https://doi.org/10.1180/emu-notes.7.1

Korenaga, J. (2017). On the extent of mantle hydration caused by plate bending. *Earth and Planetary Science Letters*, *457*, 1–9. https://doi.org/10.1016/j.epsl.2016.10.011

Li, X. P., Rahn, M., & Bucher, K. (2004). Serpentinites of the Zermatt-Saas ophiolite complex and their texture evolution. *Journal of Metamorphic Geology*, *22*(3), 159–177. https://doi.org/10.1111/j.1525-1314.2004.00503.x

Liu, C., Wang, D., Zheng, H., & Liu, T. (2017). A dehydroxylation kinetics study of brucite Mg(OH)2 at elevated pressure and temperature. *Physics and Chemistry of Minerals*, *44*(4), 297–306. https://doi.org/10.1007/s00269-016-0857-y

Liu, H., Hu, J., Xu, J., Liu, Z., Shu, J., Mao, H. K., & Chen, J. (2004). Phase transition and compression behavior of gibbsite under high-pressure. *Physics and Chemistry of Minerals*, *31*(4), 240–246. https://doi.org/10.1007/s00269-004-0390-2

Magni, V., Bouilhol, P., & van Hunen, J. (2014). Deep water recycling through time. *Geochemistry, Geophysics, Geosystems*, *15*(11), 4203–4216. https://doi.org/10.1002/2014GC005525.Received

Manning, C. E., & Ingebritsen, S. E. (1999). Permeability of the continental crust: Implications of geothermal data and metamorphic systems. *Reviews of Geophysics*, *37*(1), 127–150. https://doi.org/10.1029/1998RG900002

Menzel, M. D., Garrido, C. J., & López Sánchez-Vizcaíno, V. (2020). Fluid-mediated carbon release from serpentinite-hosted carbonates during dehydration of antigorite-serpentinite in subduction zones. *Earth and Planetary Science Letters*, *531*, 115964. https://doi.org/10.1016/j.epsl.2019.115964

Menzel, M. D., Marchesi, C., Garrido, C. J., & Hidas, K. (2019). Subduction metamorphism of serpentinite-hosted carbonates beyond antigorite-serpentinite dehydration (Nevado-Filábride Complex, Spain). *Journal of Metamorphic Geology*, *37*(5), 1–35. https://doi.org/10.1111/jmg.12481

Mercury, J. M. R., Pena, P., De Aza, A. H., Sheptyakov, D., & Turrillas, X. (2006). On the decomposition of synthetic gibbsite studied by neutron thermodiffractometry. *Journal of the American Ceramic Society*, *89*(12), 3728–3733. https://doi.org/10.1111/j.1551-2916.2006.01191.x

Merkulova, M., Muñoz, M., Vidal, O., & Brunet, F. (2016). Role of iron content on serpentinite dehydration depth in subduction zones: Experiments and thermodynamic modeling. *Lithos*, *264*, 441–452. https://doi.org/10.1016/j.lithos.2016.09.007

Okada, T., Utsumi, W., Kaneko, H., Yamakata, M., & Shimomura, O. (2002). In situ X-ray observations of the decomposition of brucite and the graphite-diamond conversion in aqueous fluid at high pressure and temperature. *Physics and Chemistry of Minerals*, *29*(7), 439–445. https://doi.org/10.1007/s00269-002-0254-6

Okazaki, K., Katayama, I., & Noda, H. (2013). Shear-induced permeability anisotropy of simulated serpentinite gouge produced by triaxial deformation experiments. *Geophysical Research Letters*, *40*(7), 1290–1294. https://doi.org/10.1002/grl.50302

Otsu, N. (1979). A threshold selection method from gray-level histograms. *IEEE Transaction on Systems, Man and Cybernetics*, *20*(1), 62–66. https://doi.org/10.1109/tsmc.1979.4310076

Padrón-Navarta, J. A., Sánchez-Vizcaíno, V. L., Hermann, J., Connolly, J. A. D., Garrido, C. J., Gómez-Pugnaire, M. T., & Marchesi, C. (2013). Tschermak's substitution in antigorite and consequences for phase relations and water liberation in high-grade serpentinites. *Lithos*, *178*, 186–196. https://doi.org/10.1016/j.lithos.2013.02.001

Peacock, S. M. (1990). Fluid processes in subduction zones. *Science*, *248*(4953), 329–337. https://doi.org/10.1126/science.248.4953.329

Perrillat, J.-P., Daniel, I., Koga, K. T., Reynard, B., Cardon, H., & Crichton, W. A. (2005). Kinetics of antigorite dehydration: A real-time X-ray diffraction study. *Earth and Planetary Science Letters*, *236*(3–4), 899–913. https://doi.org/10.1016/j.epsl.2005.06.006

Plümper, O., Botan, A., Los, C., Liu, Y., Malthe-Sørenssen, A., & Jamtveit, B. (2017). Fluid-driven metamorphism of the continental crust governed by nanoscale fluid flow. *Nature Geoscience*, *10*(9), 685–690. https://doi.org/10.1038/ngeo3009

Plümper, O., John, T., Podladchikov, Y. Y., Vrijmoed, J. C., & Scambelluri, M. (2017). Fluid escape from subduction zones controlled by channel-forming reactive porosity. *Nature Geoscience*, *10*(2), 150–156. https://doi.org/10.1038/ngeo2865

Reynard, B. (2013). Serpentine in active subduction zones. *Lithos*, *178*, 171–185. https://doi.org/10.1016/j.lithos.2012.10.012

Rüpke, L. H., Morgan, J. P., Hort, M., & Connolly, J. A. D. (2004). Serpentine and the subduction zone water cycle. *Earth and Planetary Science Letters*, *223*(1–2), 17–34. https://doi.org/10.1016/j.epsl.2004.04.018

Schmidt, M. W., & Poli, S. (2014). 4.19: Devolatilization during subduction. In H. D. Holland & K. K. Turekian (Eds.), *Treatise on geochemistry* (2nd ed., pp. 669–701). Elsevier Ltd. https://doi.org/10.1016/B978-0-08-095975-7.00321-1

Schwartz, S., Allemand, P., & Guillot, S. (2001). Numerical model of the effect of serpentinites on the exhumation of eclogitic rocks: Insights from the Monviso ophiolitic massif (Western Alps). *Tectonophysics*, *342*(1–2), 193–206. https://doi.org/10.1016/s0040-1951(01)00162-7

Tenthorey, E., & Cox, S. F. (2003). Reaction-enhanced permeability during serpentinite dehydration. *Geology*, *31*(10), 921–924. https://doi.org/10.1130/G19724.1

Tian, M., Katz, R. F., Rees Jones, D. W., & May, D. A. (2019). Devolatilization of subducting slabs, Part II: Volatile fluxes and storage. *Geochemistry, Geophysics, Geosystems*, *20*(12), 6199–6222. https://doi.org/10.1029/2019GC008489

Uesugi, K., Hoshino, M., Takeuchi, A., Suzuki, Y., & Yagi, N. (2012). Development of fast and high throughput tomography using CMOS image detector at SPring-8. In *Developments in X-Ray Tomography* (Vol. VIII, p. 8506). https://doi.org/10.1117/12.929575

Ulmer, P., & Trommsdorff, V. (1995). Serpentine stability to mantle depths and subduction-related magmatism. *Science*, *268*(5212), 858–861. https://doi.org/10.1126/science.268.5212.858

Ulmer, P., Trommsdorff, V., & Reusser, E. (1994). Experimental investigation of antigorite stability to 80 kbar. *Mineralogical Magazine*, *58A*(2), 918–919. https://doi.org/10.1180/minmag.1994.58A.2.213

van Keken, P. E., Hacker, B. R., Syracuse, E. M., & Abers, G. A. (2011). Subduction factory: 4. Depth dependent flux of H_2O from subducting slabs worldwide. *Journal of Geophysical Research*, *116*(B1), B01401. https://doi.org/10.1029/2010JB007922

von Seckendorff, V., & O'Neill, H. S. C. (1993). An experimental study on Fe-Mg partitioning between olivine and orthopyroxene at 1173, 1273 and 1473 K and 1.6 GPa. *Contributions to Mineralogy and Petrology*, *113*(2), 196–207. https://doi.org/10.14173/j.cnki.hnhg.2011.01.021

Whitney, D. L., & Evans, B. W. (2010). Abbreviations for names of rock-forming minerals. *American Mineralogist*, *95*(1), 185–187. https://doi.org/10.2138/am.2010.3371

References From the Supporting Information

Abramson, E. H. (2007). Viscosity of water measured to pressures of 6 GPa and temperatures of 300°C. *Physical Review E: Statistical, Nonlinear, and Soft Matter Physics*, *76*(5), 1–6. https://doi.org/10.1103/PhysRevE.76.051203

Audétat, A., & Keppler, H. (2004). Viscosity of fluids in subduction zones. *Science*, *303*(5657), 513–516. https://doi.org/10.1126/science.109228

Crameri, F. (2018). Geodynamic diagnostics, scientific visualisation and StagLab 3.0. *Geoscientific Model Development*, *11*(6), 2541–2562. https://doi.org/10.5194/gmd-11-254

Hack, A. C., & Thompson, A. B. (2011). Density and viscosity of hydrous magmas and related fluids and their role in subduction zone processes. *Journal of Petrology*, *52*(7–8), 1333–1362. https://doi.org/10.1093/petrology/egq048

Huang, Y., Guo, H., Nakatani, T., Uesugi, K., Nakamura, M., & Keppler, H. (2021). Electrical conductivity in texturally equilibrated fluid-bearing forsterite aggregates at 800°C and 1 GPa: Implications for the high electrical conductivity anomalies in mantle wedges. *Journal of Geophysical Research: Solid Earth*, *126*(4), e2020JB021343. https://doi.org/10.1029/2020JB021343

Pitzer, K. S., & Sterner, S. M. (1995). Equations of state valid continuously from zero to extreme pressures with H_2O and CO_2 as examples. *International Journal of Thermophysics*, *16*(2), 511–518. https://doi.org/10.1007/bf01441917